Experiments and modelling on ASDEX Upgrade and WEST in support of tool development for tokamak reactor armour melting assessments

S. Ratynskaia, K. Paschalidis, P. Tolias, K. Krieger, Yann Corre, M. Balden, M. Faitsch, Alex Grosjean, Quentin Tichit, R.A. Pitts

Nuclear Materials and Energy 33 (2022) 101303

Contents lists available at ScienceDirect

Nuclear Materials and Energy

journal homepage: www.elsevier.com/locate/nme

Experiments and modelling on ASDEX Upgrade and WEST in support of tool development for tokamak reactor armour melting assessments

S. Ratynskaia [a,*], K. Paschalidis [a], P. Tolias [a], K. Krieger [b], Y. Corre [c], M. Balden [b], M. Faitsch [b], A. Grosjean [c], Q. Tichit [c], R.A. Pitts [d], the ASDEX-Upgrade team [1], the WEST team [2], the Eurofusion MST1 team [3]

[a] Space and Plasma Physics - KTH Royal Institute of Technology, Teknikringen 31, 10044 Stockholm, Sweden
[b] Max–Planck-Institut für Plasmaphysik, Boltzmannstraße 2, D-85748 Garching, Germany
[c] CEA, Institute for Research on Fusion by Magnetic Confinement, 13108 St-Paul-Lez-Durance, France
[d] ITER Organization, Route de Vinon-sur-Verdon, CS 90 046, 13067 St Paul Lez Durance Cedex, France

ARTICLE INFO

Keywords:
Tungsten melting
Melt motion
Thermionic emission
MEMENTO code
MEMOS-U model
Active cooling

ABSTRACT

The risk of metallic armour melting constitutes a major concern for ITER and DEMO. Combined computational and experimental effort has led to a successful understanding of melt dynamics in present-day tokamaks, but there remain unexplored melting regimes of relevance to future reactors. Analysis of recent poor-versus-efficient thermionic emitter sample exposures in ASDEX-Upgrade and ITER-like actively cooled tungsten leading edge exposures in WEST is presented. The coupled thermal response and melt dynamics is modelled with the new MEMENTO code employing the MEMOS-U physics model which has no adjustable parameters. In the weak Lorentz force regime accessed in the exposures, very close agreement between modelling and experiments is achieved not only for the deformation profiles, but also for the additional, unique to these experiments, constraints; simultaneous thermal response of two different materials in ASDEX-Upgrade and *in-situ* detection of melt build-up in WEST.

1. Introduction

Liquid tungsten (W) is a powerful stable thermionic emitter owing to its relatively low work function and very low vapour pressure. Thermionic emission (TE) from a molten W surface triggers the replacement current density that is responsible for the volumetric Lorentz force that drives melt motion in tokamak W melting experiments, as first recognized in TEXTOR [1] and later confirmed in JET and ASDEX-Upgrade (AUG) [2]. The fact that TE is a potent cooling channel, controlling the quantity of melt produced and the nature of melting (transient or sustained), has recently been revealed [3,4]. The intricate role of TE in melt generation and dynamics is further complicated by the stringent constraint on the current density that is transmitted through a space-charge limited sheath [5–8].

The TE description employed in the MEMOS-U physics model [3,4,9], developed for macroscopic melt motion in fusion relevant scenarios, has been tested in multiple experiments. The scenarios modelled include the melting of W leading edges in the AUG and JET tokamaks [3,9], of a sloped geometry W sample in AUG [10] as well as of an electrically insulated W leading edge in AUG [4]; the latter featuring an unusual energy deposition due to the temporal evolution of the sheath heat transmission coefficient [4].

The modelling of macroscopic melt motion in present-day tokamaks has proven to be very successful, but there are W melting regimes which have hitherto remained unexplored in experiments. Furthermore, the direct detection of thermionic emission and/or its effects is desirable given the TE importance in melt formation and dynamics and the fact that comparison with observations is typically with the final surface deformation profiles [3,4,9]. Such detection has been attempted previously in two AUG experiments, involving thermionic current measurements [11] and an electrically insulated (floating) sample [4]. In the former experiment, the interference from a component of the electric current originating from elsewhere along with the excess of the measurement system saturation level have impeded direct comparison

* Corresponding author.
E-mail address: srat@kth.se (S. Ratynskaia).
[1] See the author list of U. Stroth et al. 2022 Nucl. Fusion **62** 042006.
[2] See http://west.cea.fr/WESTteam.
[3] See the author list of Labit et al. 2019 Nucl. Fusion **59** 0860204.

https://doi.org/10.1016/j.nme.2022.101303
Received 30 July 2022; Received in revised form 12 October 2022; Accepted 9 November 2022
Available online 19 November 2022

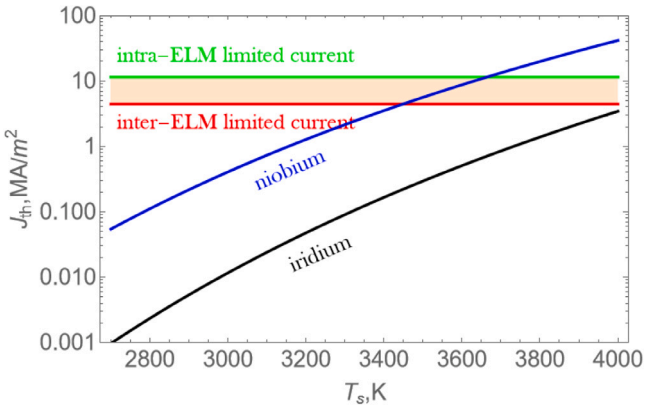

Fig. 1. Escaping thermionic current density from Ir and Nb as a function of the surface temperature for the leading edge geometry (for magnetic field normal to the surface). The space-charge limited values are evaluated for typical AUG intra- and inter-ELM plasma conditions as in Refs. [6,7].

with the modelled thermionic emission current density [12]. In the latter experiment, it was anticipated that, despite TE emission, the floating W sample should exhibit no melt displacement due to the absence of a replacement current flowing through the melt layer and thus of the dominant Lorentz force. The experiment showed, however, that the floating sample received about 30% more energy compared to an identical grounded sample, resulting in sustained melting and appreciable melt displacement due to (the typically negligible) acceleration by gravity [4].

Here, we analyse two new deliberate melting experiments which have realized unexplored regimes; melting of poor-versus-efficient thermionic emitters in AUG and sustained melting on an actively cooled W component in WEST, where the same technology as foreseen in the ITER divertor [13] is utilized. The experiments have yielded new empirical evidence that provide a stringent test of the TE description in the MEMOS-U melt motion model. The MEMOS-U physics model has been recently implemented in a new code, **MEMENTO** (**ME**tallic **M**elt **E**volution in **N**ext-step **TO**kamaks). The code utilizes non-uniform and adaptive meshing along with sub-cycling in time enabled by the AMReX open-source framework [14,15] as well as by AMReX's built-in parallelization capabilities. All the simulations presented here were carried out with the MEMENTO code, with the exception of the predictive studies reported in Sec.2.1, that were performed with the MEMOS-U code prior to the actual experiment.

2. "Poor versus efficient thermionic emitter" exposure in AUG

2.1. Experiment design

For design and preparation of the new experiment, MEMOS-U simulations have been employed to explore melting regimes and to find an optimal exposure geometry. The main idea behind the experiment is to contrast the deformation profile of a poor (high work function, W_f) to that of an efficient (low W_f) thermionic emitter, which otherwise have similar thermophysical properties, following exposure to the same ELMing H-mode plasma. Given the large difference in the resulting Lorentz force, one can anticipate negligible melt displacement in the case of the poor emitter and significant deformation in the case of the efficient emitter.

Amongst the elemental metals which are acceptable for exposure in a deliberate tokamak melting experiment, the best candidate pair is iridium (Ir, W_f = 5.3 eV) and niobium (Nb, W_f = 4.2 eV). In fact, given the exponential dependence of the Richardson–Dushman formula, as discerned from Fig. 1, the thermionic current densities for Ir and Nb differ about two orders of magnitude prior to the space charge limited regime. The materials have nearly identical melting points, with 2719 K for Ir and 2745 K for Nb and relatively close though not identical thermophysical properties; the Nb thermal diffusivity at room temperature is about half of that of Ir while at elevated temperatures they become nearly identical. With the excess thermionic cooling from Nb (compared to Ir), a similar thermal response was anticipated, but this also depends on the heat flux specifics. In particular, detailed calculations revealed that the Nb sample would melt much more easily than its Ir partner under plasma exposure.

In order to model this experiment, the material library of MEMOS-U and MEMENTO that is naturally focused on tungsten [16] and beryllium [17] had to be extended. The analytical expressions adopted for the temperature dependence of the thermophysical properties of iridium and niobium are freely available online [18].

The limited current density is the same for both metals, since it only slightly depends on the TE electron energy distribution which is independent of the work function [6]. Thus, it is crucial to stay away from the transition to the space charge limited regime, *i.e.* to operate at lower surface temperatures where there is no virtual cathode formation and the Richardson–Dushman formula is valid. MEMOS-U simulations have been carried out for several sample geometries, employing the heat flux reconstructed from IR thermography in AUG discharge #33511 from a previous tungsten melt study [11]. The simulations revealed that leading edge and large angle slopes lead to excessively high surface temperatures (and, hence, vapour production) and emission in the limited regime. As a result, the 17° slope geometry was suggested as optimal, for which MEMOS-U modelling predicted the formation of a modest Ir molten pool with small displacement and exaggerated melt formation and deformation of the Nb sample, with possible melt ejection from the sample edge.

2.2. Experiment realization

Ir and Nb samples were simultaneously exposed to five ELMing H-mode discharges #39176 – 39180 at the outer divertor target plate using the divertor manipulator II DIM-II system [19] (see also Fig. 1, 2 of Ref. [11] for details of DIM-II). The discharge parameters were; P = 2.5 MW (NBI), 4.6 MW (ECRH), I_p = 1 MA and B_t = −2.5 T. The geometry and dimensions of the sloped samples is shown in Fig. 3.

The exposure duration was increased step-wise in successive, otherwise identical, discharges and high-resolution photographs of the two samples were taken after each discharge, see Fig. 2. Visual inspection confirmed the thermal responses and melt displacements predicted by the MEMOS-U modelling; the Nb sample melts more easily and exhibits severe deformation with melt spilling, while the Ir sample melted only after the longest (#39180) exposure with a modestly displaced pool.

2.3. Modelling results

2.3.1. Experimental heat flux and sample loading

The last and longest discharge #39180 that led to Ir melting, is discussed in what follows. The heat flux at the sample location is reconstructed from the standard IR thermography diagnostic in a sector toroidally ~ 180° away from the manipulator exposure position. The flux features negative values after ELM incidence over ~ 35% of the data due to a mismatch between the emissivity and thermal diffusivity assumed in the THEODOR code used for reconstruction of the power flux and the actual unknown emissivity and thermal diffusivity of the tungsten tile surface observed by the IR diagnostic. The negative values are removed and substituted by the heat flux from the analytical fit to the inter-ELM spatial profile recovered by the IR data. This adds an energy of ~ 20%, as determined by integrating the heat flux over the wetted surface and over the exposure time prior to and after the negative value correction. A corresponding reduction coefficient has not been introduced, since, as discussed below, the empirical heat flux appears to be underestimated and will be increased further to match

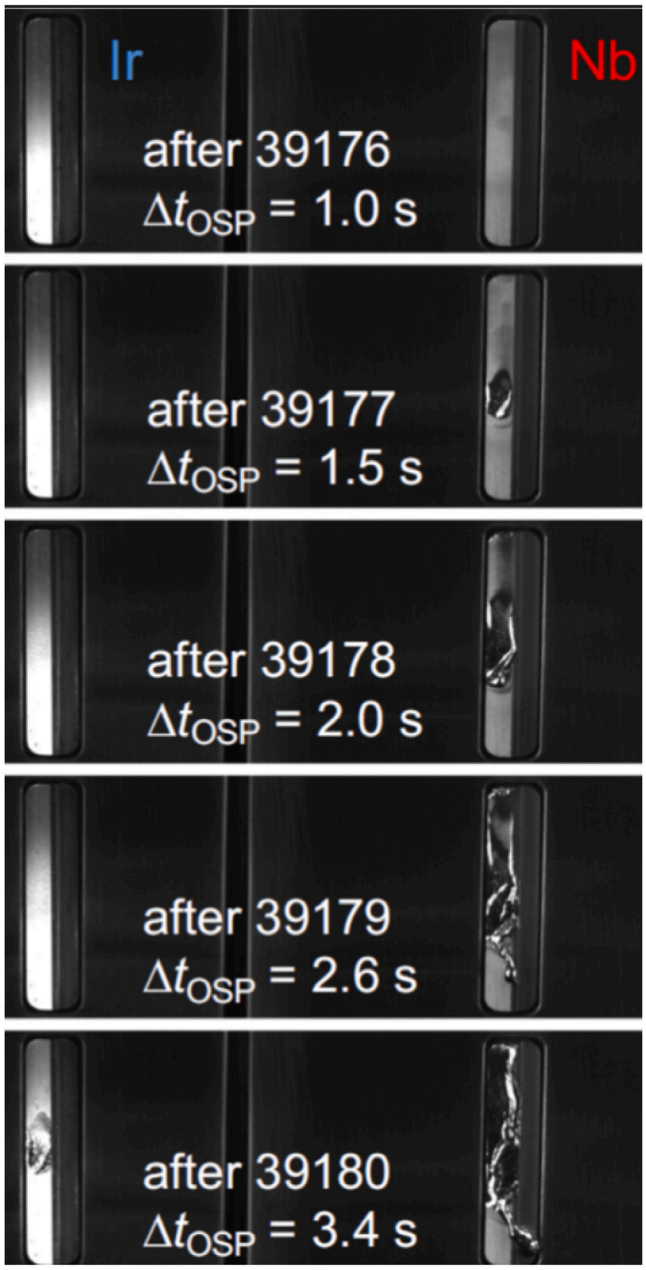

Fig. 2. High resolution images of the Ir and Nb samples after each of the four consecutive exposures of increasing duration ELMing H-mode in the AUG outer divertor. The sample length is 39 mm, for 3D geometry refer to Fig. 3. The duration of *steady* outer strike point Δt_{OSP} is indicated in the images — the overall exposure is longer, see Sec.2.3.2 for details.

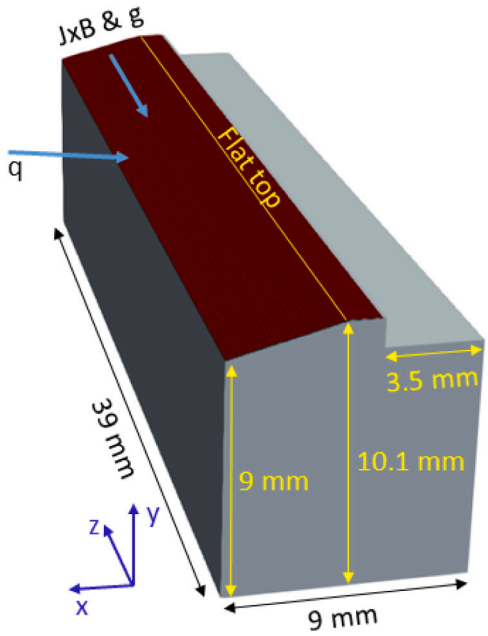

Fig. 3. The 3D geometry of the sloped AUG Ir and Nb samples together with the heat flux loading (in red). The dimensions of the flat top and the step height, are 1 mm and 1.1 mm, respectively. The directions of the incident plasma heat flux, Lorentz force and gravity are sketched. The coordinate system is also indicated. (For interpretation of the references to colour in this figure legend, the reader is referred to the web version of this article.)

the observed melting volumes. In fact, the modest $\lesssim 600\,\mathrm{MW/m^2}$ and $\sim 70\,\mathrm{MW/m^2}$ values of the maximum measured intra-ELM and inter-ELM field-parallel heat fluxes (which become $\lesssim 500\,\mathrm{MW/m^2}$ and $\sim 60\,\mathrm{MW/m^2}$, when accounting for the correction necessary to preserve the overall deposited energy after the removal of negative values) are not sufficient to induce melting over the exposure duration.

Although the IR-recovered power flux relies on the total energy balance as determined from the long time observations, the details of energy deposition on short time scales might suffer from different inaccuracies. Indeed, the sampling time of the IR camera may introduce an underestimation of the intra-ELM values by $\sim$ 20%, while the reconstruction of ELM values also involves three not-well-constrained fitting parameters. This implies that even when the overall deposited energy corresponds to the actual value, the sample thermal response is not necessarily reproduced in fine detail since the energy deposition time scale plays a role in approaching the melting point, in particular, the efficient contribution of the large intra-ELM surface temperature excursions. The assessment of the overall deposited energy uncertainty, as recovered by IR thermography, can be facilitated by a comparison with thermo-couple (TC) data from the outer divertor. In the discharge analysed here, the total energy onto the entire lower divertor is 3.8 MJ as determined by the IR measurements and 4.8 MJ as determined by the TC data. Accounting for the symmetric TC data error-bar of $\sim$ 20%, this translates to a possible underestimation of the IR-recovered power flux up to $\sim$ 50%.

We restrict the analysis to loading in the optical approximation; this way to induce Ir melting the experimental heat flux needs to be further increased by $\sim$ 40%. It is worth underlining that this flux deposition strategy underestimates the overall energy received by the sample. The geometry of the sample (Fig. 3) features a flat top at the end of the sloped surface, which forms a step with a shadowed flat surface behind. The order of mm dimensions of the flat top and the step height are comparable to the ion Larmor radius, indicating that the optical approximation is not accurate, at least not for the power carried by ions. Furthermore, detailed PIC simulations of gap loading have revealed that edges and magnetically shadowed regions can also receive heat flux, in particular due to the effect of strong sheath electrostatic fields on ions as well as the 3D effect of the ExB drift on electron transport [20,21]. Clearly, such complexity of 3D sample loading is not possible to capture with the experimental field-parallel heat flux as the only input.

Since it is difficult to assess the accuracy of the empirical heat flux input in a detailed manner, the goal is to satisfy all available experimental constraints *simultaneously*. In particular, with the same heat flux, we aim to match the thermal responses of both Ir and Nb as well as the different timing of non-negligible melt formation and displacement for both materials, as revealed by the successive exposures with stepwise increased duration. Finally, note that, as reported in Refs. [3,9],

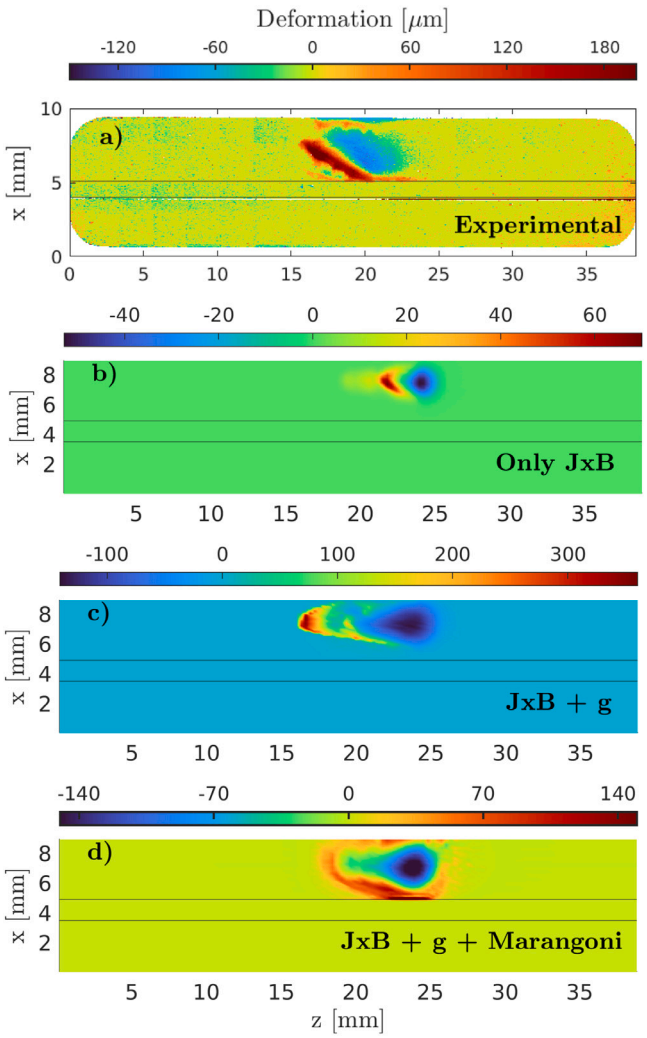

Fig. 4. Ir deformation profiles; (a) profilometry of exposed sample, (b) MEMENTO modelling with the Lorentz force, (c) MEMENTO modelling with the Lorentz force and gravity, (d) MEMENTO modelling with all forcing terms. Zero deformation refers to the unaltered sample shape. For the coordinate system refer to Fig. 3. (For interpretation of the references to colour in this figure legend, the reader is referred to the web version of this article.)

the melt volume is highly sensitive to small heat flux variations, since only a minuscule amount of the total energy is expended on the phase transition. To be more specific, only 4 J out of 16 kJ absorbed is needed to melt the observed $\sim 1\text{mm}^3$ of Ir.

2.3.2. Thermal response of Ir versus Nb

Both the Ir and Nb samples are loaded as specified above, with only a variation in the loading duration. The Ir sample was loaded for 4 s with 3.4 s of steady outer strike point (OSP), as indicated in Fig. 2, which is the duration of the pulse #39180 in which Ir melting occurred. The Nb sample was loaded only for 2 s with 1.5 s of steady OSP, as indicated in Fig. 2, relevant to the exposure to pulse #39177, where Nb first melted. The modelling of the Nb follow-up exposures is restricted due to the fact that the deformed sample was re-melted in three more discharges. As evident from the series of images shown in Fig. 2, this implies a continuously changing topology and projected area, as well as sloped and curved bathymetry effects. These lie beyond the applicability of the shallow water approximation that is the core of the MEMOS-U physics model, since the spatial alignment of the melt layer was varying in time.

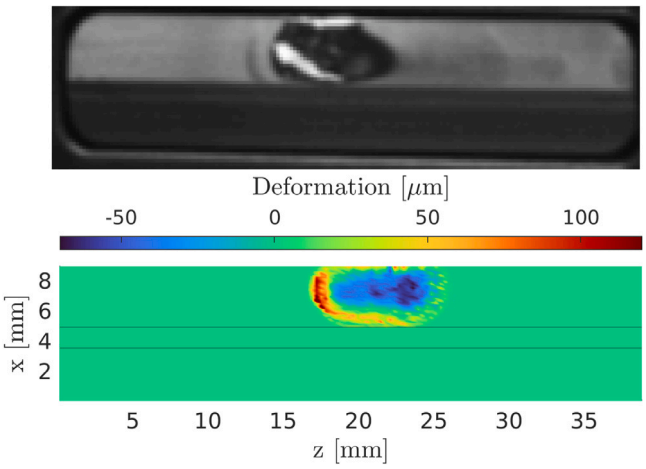

Fig. 5. The experimental profile of the Nb sample after exposure to #39177 (as in Fig. 2). MEMENTO results for the Nb surface deformation profile after 2 s of exposure. For the coordinate system refer to Fig. 3. Note the alignment of the craters in experimental and modelling images is well within the uncertainty of the spatial profile of heat deposition along the sample (~ 1 cm). (For interpretation of the references to colour in this figure legend, the reader is referred to the web version of this article.)

On the Nb sample, occasional and very short-lived (< 10 ms) transient pools started to appear at around 1.4 s and the melting became sustained from 1.8 s. The melt surface temperature remained close to 2800 K, which is just above the Nb melting point of 2745 K. At such temperatures, the Richardson–Dushman current density of Nb is close to 0.1 MA/m^2 (see Fig. 1). The instantaneous Nb melt depth reached ~ 100 μm.

As presented in Section 2.1 and consistent with the experimental results, Ir is more difficult to melt. The simulations revealed that occasional and very short-lived (< 10 ms) transient pools on the Ir sample started to appear around 2.7 s and that melting became sustained towards the end of the exposure, from 3.5 s. The pool surface temperature remains at about 2825 K, which is again not far from the melting point of 2719 K. At these temperatures, the Richardson–Dushman current density of Ir is close to 3 kA/m^2. The instantaneous Ir melt depth reached ~ 80 μm.

2.3.3. Melt dynamics and deformation profiles

In previous melt experiments the JxB acceleration mechanism was by far dominant over accelerations due to gravity and thermo-capillary effects [3,4,9]. This is not the case in the scenarios modelled here. We briefly recap the origin of the thermo-capillary flow before proceeding with the presentation of the results for Ir followed by those for Nb.

The free surface jump in the tangential components of the hydrodynamic stress is balanced by the stress due to tangential gradients in the surface tension, $\nabla_t\sigma$. A non-zero $\nabla_t\sigma$ at the interface, stemming from variations in the surface temperature or chemical composition, is able to drive melt motion. For uniform material composition of relevance to fusion applications, $\nabla_t\sigma$ becomes the thermo-capillary term $\partial\sigma/\partial T\nabla_t T_s$. Since surface tension decreases with increasing temperature, the effective force on the metallic melt layer pushes the liquid metal from hot regions towards colder areas, *i.e.* the Marangoni effect.

In the W leading edge (LE) experiments in AUG and JET, the JxB force density is two orders of magnitude larger than the gravitational force density $\rho_m g$ [3,9], where ρ_m is the mass density. The role of gravity was clearly observed only in the AUG floating W LE exposure, where no current was passing through the liquid volume [4]. Thermo-capillary acceleration, while omnipresent, does not usually lead to noticeable bulk displacements, since tangential gradients are weak and it cannot compete in magnitude with the dominant acceleration due to JxB force [3,4,9]. However, given the low relevant melting points

(below 2750 K for Ir, Nb vs 3695 K for W), the corresponding TE current density in this experiment is nearly two and four orders of magnitude lower for Nb and Ir, respectively, than for W. Thus, the secondary acceleration mechanisms of gravity and Marangoni flows can now be observable.

In fact, the profilometry of the exposed Ir sample in Fig. 4(a) clearly shows that the melt is pushed towards the edge and the flat top, so that an inclined ridge of frozen melt is formed by the displaced liquid. It is worth noting that, since the deformation is very small, the non-perfect sample alignment has an impact on the accuracy of the measured profile; the order of magnitude dimensions of the crater and the ridge are reliable, but the dimensions of the smaller features are more uncertain. The excavated volume estimates yield ~ 0.75 mm^3.

To demonstrate the effect of each force on the melt dynamics, we added the relevant source terms $J \times B$, $\rho_m g$ and $(3/2h)(\partial\sigma/\partial T)\nabla_t T_s$ sequentially in the momentum balance equation, as formulated by Eq. (2) of Ref. [4]. Here, h denotes the melt layer thickness. The projected final deformations are presented in Figs. 4(b-d). For the 3D geometry refer to Fig. 3. All runs were performed with the same heat flux loading. Fig. 4(b) shows the profile when the melt is accelerated only by the JxB force. The displacement is non-uniform and it leads to a rather localized build up (displaced volume of ~ 0.13 mm^3). Gravity points downwards along the tile surface, in the same direction as JxB, and provides an acceleration $g\cos(15°)$ taking into account the tile inclination against the vertical. When gravity, which is 25 times larger than $J \times B/\rho_m$, is added, the immediate effect is about 7-fold increase in the melt volume as observed in Fig. 4(c) (note the difference in the colour coding scale). Since the runs are identical with the exception of the enhanced flow, this is a clear indication of the role of convection in the thermal response, whose importance has been pointed out in the modelling of previous melt experiments [3,4,9]. The displacement and build up are more uniform now, though some reflection of the pool shape can still be seen. Finally, Fig. 4(d) shows results with the thermo-capillary term added. Since the flat top is the coldest part of the sample, there is appreciable flow towards it and the final deformation profile (d) now reproduces the main features of the experimental profile (a), with the inclined frozen ridge and also some small material accumulation at the edge and sides. The excavated volume is ~ 0.95 mm^3, matching well the experimental observations. In the case (d), the melt is accelerated to ~ 10 cm/s.

We now turn our attention to the Nb deformation profiles formed after 2 s of exposure to the same heat flux, as presented in Fig. 5. For Nb, the JxB acceleration is 1.5 times higher than the gravitational acceleration with the thermo-capillary term pushing the melt away from the hottest spots as before. The resulting acceleration leads to velocities of ~ 10 cm/s. With in-situ high resolution images taken after each discharge, the image of the Nb sample after exposure to #39177 is available (Fig. 2) for comparison with modelling results. Naturally, only tangential dimensions of the deformation can be compared — no information on the depth/height and the excavated volume can be deduced from the image.

While the melt pool life-time is the relevant figure of merit for the velocity evolution due to acceleration by Lorentz force and gravity, this is not the case for Marangoni flows. The temperature gradients are localized in space and time as they continuously change due to the melt motion and displacement but also due to spatial and temporal variations of the intra-ELM heat flux. Thus, while the thermo-capillary term might attain rather high values locally, the corresponding acceleration times are restricted to much shorter periods. The similar Ir and Nb melt velocities can be largely explained by the different life-times (onset of sustained melting vs. exposure time, presented in Section 2.3.2) and the different values of $(J \times B)/(\rho_m g)$.

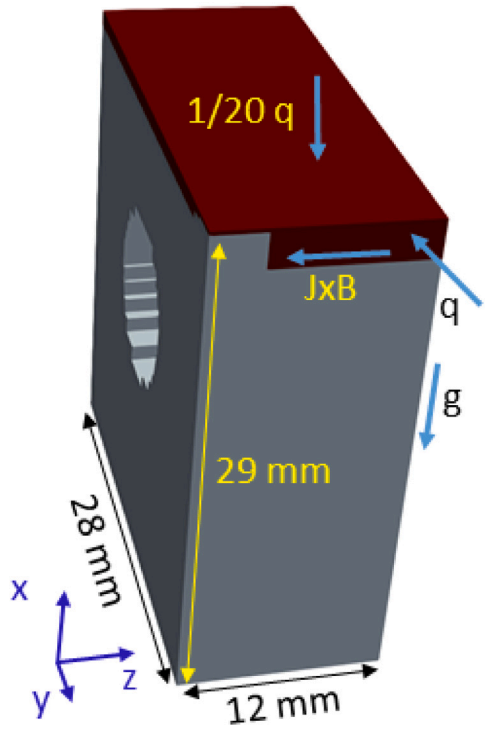

Fig. 6. The 3D geometry of the exposed actively cooled WEST W monoblock together with the heat flux loading (in red). The small and large dimensions of the LE wetted area are 0.3 mm (left) and 2.3 mm (right). The directions of the incident plasma heat flux, Lorentz force and gravity are sketched. The coordinate system is also indicated. (For interpretation of the references to colour in this figure legend, the reader is referred to the web version of this article.)

3. ITER-like actively cooled W leading edge exposure in WEST

3.1. Experiment

Controlled sustained W-melting on a poloidal sharp leading edge, introduced into a W monoblock (MB) on one of the actively cooled ITER-like plasma-facing units (PFU) in the lower divertor, has been achieved in the WEST tokamak [22]. Full experimental details are provided in Ref. [22] and here we repeat only the basic points. A groove (30 mm long toroidally, 9 mm wide poloidally, and 2 mm deep) was machined in one of the MBs on one PFU in order to expose the sharp LE of the adjacent downstream MB directly to the full incident parallel heat flux q, see Fig. 6. The W LE was exposed in steady-state L-mode plasma discharges, #56540 – 56542, 5 s long each. The X-point height was adjusted pulse to pulse in order to keep the maximum heat flux in the centre of the groove.

We highlight a unique feature of this experiment; high spatial resolution, 0.1 mm/pixel, IR imaging enabled the *in-situ* detection of the LE deformation which is a footprint of melt displacement. This yielded previously inaccessible information concerning melting onset and melt build-up. Moreover, it permitted the direct observation that, even though all three exposures had identical discharge parameters, an appreciable build-up formed only in one discharge (#56541). This constitutes direct empirical evidence of the fact that melt volume exhibits high sensitivity to small power variations.

3.2. Modelling results

3.2.1. Experimental heat flux and sample loading

Since melting was detected in only one discharge, it is safe to attribute the final deformation profile to the melting event in a single exposure, which is modelled here. The heat flux q as a function of the

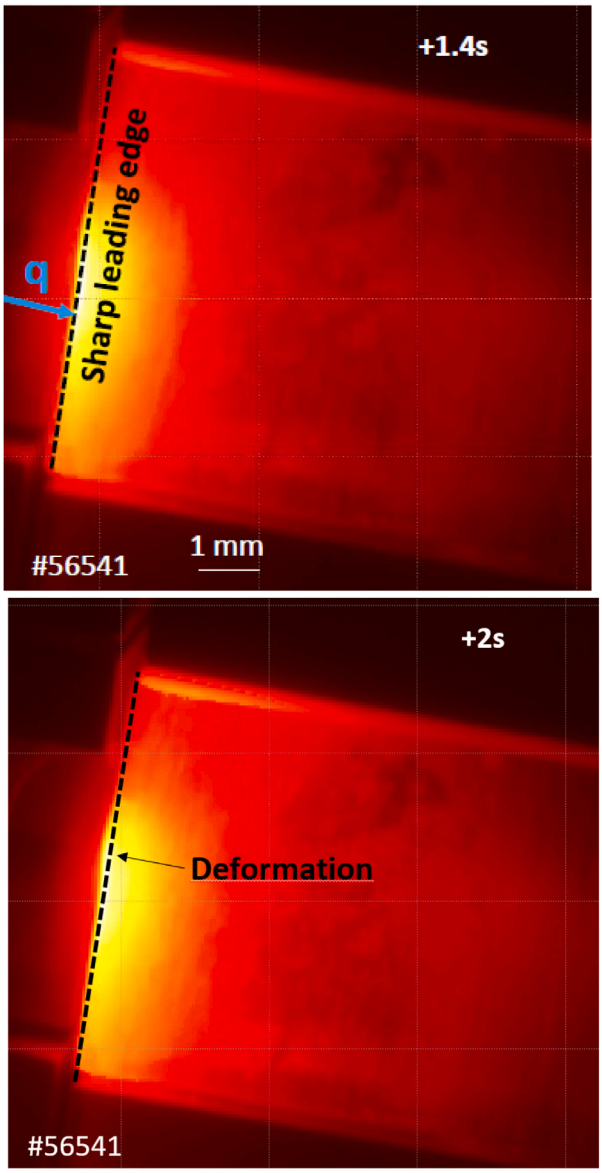

Fig. 7. *In-situ* detection of melt build-up by high spatial resolution IR imaging, before (top, at 1.4 s) and after (bottom, at 2 s) the first evidence of the leading edge deformation.

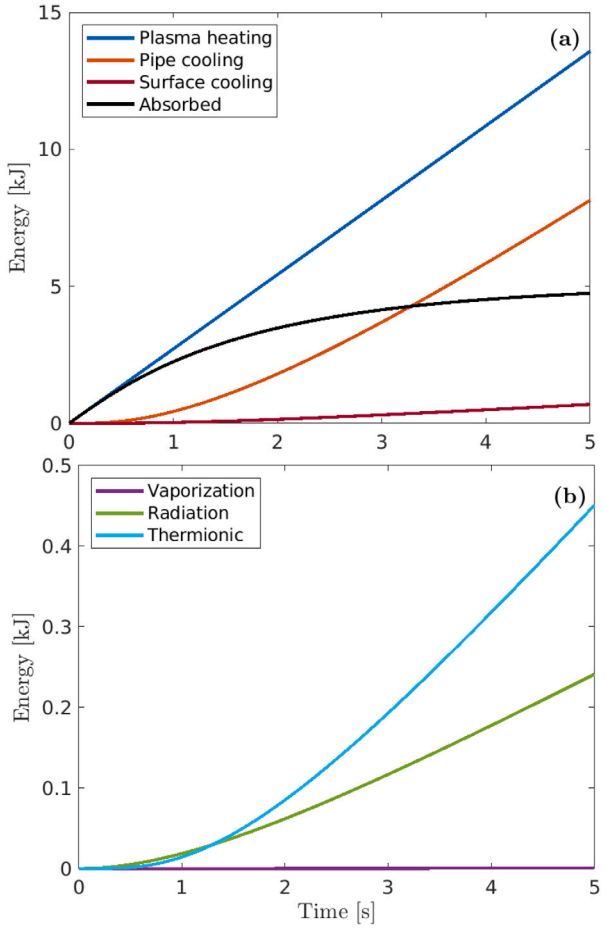

Fig. 8. MEMENTO results for the overall energy balance (a) and the surface cooling (b) during the exposure of the actively cooled WEST W monoblock. (For interpretation of the references to colour in this figure legend, the reader is referred to the web version of this article.)

z-coordinate (along the LE, see Fig. 6) is reconstructed from the IR imaging. This empirical heat flux has been matched to the analytical expression of the Eich scaling, Eq. (2) of Ref. [23], with the following parameters: $q_0 = 314\,\mathrm{MW/m^2}$, $S = 2$ mm, $\lambda_q = 2$ mm (on the target), $z_0 = 5.5$ mm. In the reconstruction, the surface cooling fluxes are not accounted for, thus the recovered heat flux is underestimated, entailing an increase by $\sim 20\%$ to induce a quantity of melt matching the observed volume. This corresponds to a loading with the maximum $q \sim 150\,\mathrm{MW/m^2}$.

The sample geometry and plasma-wetted area (in red) are shown in Fig. 6. The LE is loaded with the heat flux q as specified above, while the top of the monoblock is loaded with $q/20$ accounting for the 2.9° inclination of the incident magnetic field lines. The MB is equipped with a cooling pipe consisting of 2.5 mm thick Cu and CuCrZr layers. In the modelling of the cooling pipe, some approximations are employed that have been shown to have a minimal impact on the temperature gradients inside the pipe [24]. First, for simplicity, the Cu pipe is substituted by a 1 mm thick layer of W. Second, the radius of the pipe is reduced to account for the increase in its circumference due to the rectilinear approximation of the circular cross-section made in the MEMENTO modelling. Third, the cooling pipe is shifted so that 7 mm of W lies between the top of the MB and the coolant. The heat transfer coefficient between the flowing water and the pipe, as employed by the ITER Organization, is adopted from Ref. [24].

3.2.2. Thermal response

The MB is loaded with the above specified heat flux for 5 s. The temperatures in the vicinity of the pipe are a few hundred degrees above the coolant temperature of 343 K and with the surface temperature reaching melting point, this implies the presence of sharp gradients, with a drop of ~ 3000 K over ~ 10 mm.

MEMENTO simulations show that the surface temperature crosses the W melting point shortly after 1 s and that melt displacement throughout the remaining exposure time leads to a final deformation in the 200–300 μm range. The deformation evolves promptly over the first second of the pool life-time; it is ~ 10 μm at 1.2 s, 100 μm (crater depth) / 200 μ m (build-up height) at 2 s, subsequently growing slowly to the final values. Such an evolution is a consequence of the temperature response; the initial melt freezes quickly near the pool, while later on the melt can be displaced further tangentially thus not providing significant contributions to the build-up height. In a similar fashion, as the exposure time increases, the crater expands tangentially with depth excavation slowing down.

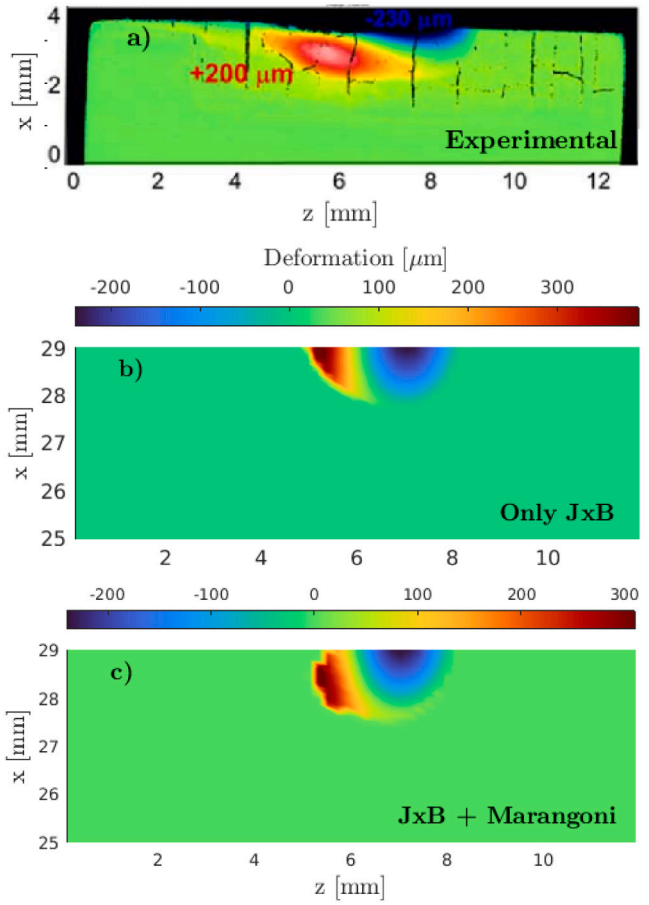

Fig. 9. W deformation profiles; (a) profilometry of the exposed LE W sample, (b) MEMENTO modelling with the Lorentz force, (c) MEMENTO modelling with the Lorentz force and thermo-capillary flows. The original profilometry image from Ref. [22] (upper plot) has been overlaid with the coordinate system employed in the MEMENTO simulations. For the coordinate system refer to Fig. 6. (For interpretation of the references to colour in this figure legend, the reader is referred to the web version of this article.)

These results are in excellent agreement with the empirical data concerning the timing of appreciable melt build-up detection. In WEST, the very high spatial resolution IR system is monitoring the temperature of the MB top surface [25]. Such system enables to monitor the variation, with submillimetre accuracy (0.175 mm typically), of the leading edge due to melt motion, as displayed in Fig. 7. As seen from the images, the deformation of the leading edge appears around 1.7±0.3 s.

Since this is the first time that simulations of both the thermal response (with all surface cooling fluxes) and melt motion of an actively cooled PFC are presented, it is instructive to discuss the energy balance aspects in detail. Fig. 8(a) presents the total energy deposited by the plasma (in blue), the energy loss due to the cooling pipe (in orange), the energy loss due to surface cooling (in red) and the energy absorbed by the sample (in black) as functions of time. It is evident that passive surface cooling represents a non-negligible 9% fraction of active cooling. The breakdown of the surface cooling energy per mechanism is depicted in Fig. 8(b), revealing that cooling due to thermionic emission is the dominant contribution. However, thermionic cooling is not drastically higher than radiative cooling (as in inertially cooled W LE experiments [3,4,9]), since the surface temperature barely exceeds the W melting point in this scenario; see the cooling fluxes in Fig. 4 of Ref. [9].

The melt pool surface temperature remains close to 3705 K and the instantaneous melt depth lies in the range of a few micrometres. These indicate that most absorbed energy is consumed to bring the W sample to the melting point. This is also clear from the fraction that is expended on the phase transition; from the 14 kJ energy that is deposited by the plasma, only 1 J is necessary to melt the observed volume of 0.26 mm^3 (as measured post-mortem with confocal microscopy [22]).

The main difference with previous passively cooled W LE experiments in JET and AUG [11,26] lies in the facts that those transient melt pools featured surface temperatures several hundred of degrees above the W melting point and that they reached depths of ~ 200 µm [3,4,9]. For comparison, the plasma incident energy and energy losses due to surface cooling for transient W LE melting in the JET experiment [26] can be found in Fig. 10 of Ref. [9].

3.2.3. Melt dynamics and deformation profiles

Fig. 9 presents the profilometry and MEMENTO modelling results for the final deformation. The images are in the LE plane. In this exposure, the direction of gravity is perpendicular to the Lorentz force and points downwards (see Fig. 6) – in the direction of the dominant Marangoni flow – since the edge (along $x = 29$ mm in Fig. 9) is the hottest region of the MB. The gravitational force is nearly two orders of magnitude lower than the JxB force and it cannot compete with the thermo-capillary term either, thus it has negligible effect on the melt dynamics and bulk displacement.

Since the surface temperature remains very close to the melting point, for the given incident heat flux, the TE current density does not enter the space-charge limited regime and still follows the Richardson–Dushman formula. With $J_{th} = 5.3\,MA/m^2$ and $B = 3.96$ T in this WEST experiment, the Lorentz force[4] is nearly identical to that induced in the transient W LE exposures in JET and AUG, where $J_{th} = 10 - 15\,MA/m^2$ and $B = 2.5 - 2.9$ T [3,9]. Given that the transient pool life-time was merely ~ 10 ms, it is striking that the sustained pools analysed here are accelerated to speeds of no more than a few cm/s and are displaced at distances of the order of mm, Fig. 9(b), in contrast to the transient pools with speeds of ~ 1 m/s and displacements of ~cm observed in the JET and AUG W LE experiments [3,9]. The reason lies in the aforementioned large melt depth difference between these two scenarios. In the WEST case, the ultra-thin ~ µm layers promptly reach their terminal speed as dictated by the balance between JxB and viscous damping which scales as $1/h^2$. Moreover, the prompt re-solidification of such layers further restricts displacements.

Comparing Figs. 9(a),(b), it can be discerned that including the JxB force alone is sufficient to reproduce the main features of the experimental profile. There is only one small aspect that is missing in profile (b); a displacement of the melt build-up away from the edge. This is captured by adding the thermo-capillary term which will push melt away from the hottest edge down to the colder areas, as shown in Fig. 9(c). The experimental excavated melt volume is also well matched by the MEMENTO simulations.

We note that fine tuning the parameters of the empirical heat flux (in particular λ_q and q_0) allows broadening of the crater to achieve an even closer match of all linear dimensions of the deformation. Such an exercise is not undertaken here, as it does not bring any further insight into the problem, nor would it modify the main conclusions given the experimental uncertainties.

4. Summary

The crucial role of thermionic emission in the energy and momentum balance of tungsten melting events calls for a thorough validation of our current understanding of the escaping current density. Two new melt experiments in AUG and WEST have accessed previously

[4] Note that in the case of the leading edge geometry, the actual current density in the JxB term is a few times smaller than the surface current density J_{th} due to the bending of the bulk current within the melt layer volume [27].

unexplored regimes allowing the impact of thermionic emission to be assessed in the interval prior to the transition to space charge limitation which was characteristic of previous deliberate W melting experiments performed on JET and AUG. Moreover, in these two new experimental scenarios, typically inaccessible in previous experiments secondary thermo-capillary effects are unmasked, owing to the uncharacteristically low contribution of the usually dominant JxB force. In addition to its direct benefit for model benchmarking, this weak JxB regime is also relevant to ELM-induced first wall plasma-facing component castellation edge melting in ITER, since the Be which will be used to armour the ITER first wall is a poor thermionic emitter.

While the matching of the final deformation profiles constitutes the principle part of the experiment-simulation comparison, the design and diagnostics of these exposures also led to experimental constraints which further enhance the value of the validation effort. In particular, in the AUG experiment, it has been shown that the MEMENTO code implementation of the MEMOS-U physics model was able to reproduce the thermal responses and deformation profiles of two different materials (Ir and Nb), which possess diametrically opposite thermionic properties, under the same experimental heat flux. Furthermore, the timing of formation of the sustained Ir melt pool revealed by the simulations entirely agrees with the results of four Ir exposures, where only the last and the longest one had induced observable melt volume and displacement. This experiment has also provided an unambiguous test of the model's predictive power; results of the initial study, carried out *prior* to the experiment, were fully confirmed in the actual exposures.

In the WEST experiment, the empirical timing of the W LE deformation detection was reproduced in the MEMENTO simulations, in addition to a close match of the final deformation profiles. The WEST experiment also provided a direct empirical confirmation of the melt volume sensitivity to minuscule power variations, as repeatedly highlighted in our previous validation activities [3,9]. This inspired the design of upcoming WEST experiments, where MEMENTO modelling predicts that a $\sim 10\%$ heat flux increase will lead to a ten-fold increase of the melt volume.

The successful reproduction of the new tokamak melt experiments adds the modelling of actively cooled W melts as well as the modelling of poor and efficient thermionic emitter melts to the growing validation list of the MEMOS-U physics model, which includes ELM-induced passively cooled W divertor melting and disruption-induced Be first wall melting, different electrical connections (grounded and floating) and multiple exposure geometries [4].

The agreement of MEMENTO modelling with these specially designed exposures lends additional confidence to our understanding of the role of thermionic emission and of secondary acceleration mechanisms. It further establishes the predictive power of the MEMOS-U physics model and the MEMENTO code for the assessment of gross topological erosion due to armour melting on ITER and DEMO.

CRediT authorship contribution statement

S. Ratynskaia: Conceptualization, Methodology, Investigation, Writing – original draft. **K. Paschalidis:** Software, Investigation, Writing – review & editing. **P. Tolias:** Conceptualization, Methodology, Writing – review & editing. **K. Krieger:** Investigation. **Y. Corre:** Investigation. **M. Balden:** Investigation. **M. Faitsch:** Investigation. **A. Grosjean:** Investigation. **Q. Tichit:** Investigation. **R.A. Pitts:** Conceptualization, Writing – review & editing.

Declaration of competing interest

The authors declare that they have no known competing financial interests or personal relationships that could have appeared to influence the work reported in this paper.

Data availability

Data will be made available on request.

Acknowledgements

SR, PT acknowledge the financial support of the Swedish Research Council under Grant No 2021-05649. The work has also been performed within the framework of the EUROfusion Consortium, funded by the European Union via the Euratom Research and Training Programme (Grant Agreement No 101052200 - EUROfusion). The views and opinions expressed are however those of the authors only and do not necessarily reflect those of the European Union, European Commission or the ITER Organization. Neither the European Union nor the European Commission can be held responsible for them.

References

[1] G. Sergienko, B. Bazylev, T. Hirai, et al., Experience with bulk tungsten test-limiters under high heat loads: melting and melt layer propagation, Phys. Scr. T128 (2007) 81–86.
[2] R.A. Pitts, S. Bardin, B. Bazylev, M.A. van den Berg, P. Bunting, S. Carpentier-Chouchana, J.W. Coenen, Y. Corre, R. Dejarnac, F. Escourbiac, J. Gaspar, J.P. Gunn, T. Hirai, S.-H. Hong, J. Horacek, D. Iglesias, M. Komm, K. Krieger, C. Lasnier, G.F. Matthews, T.W. Morgan, S. Panayotis, S. Pestchanyi, A. Podolnik, R.E. Nygren, D.L. Rudakov, G. De Temmerman, P. Vondracek, J.G. Watkins, Physics conclusions in support of ITER W divertor monoblock shaping, Nucl. Mater. Energy 12 (2017) 60–74.
[3] S. Ratynskaia, E. Thorén, P. Tolias, R.A. Pitts, K. Krieger, L. Vignitchouk, D. Iglesias, Resolidification-controlled melt dynamics under fast transient tokamak plasma loads, Nucl. Fusion 60 (2020) 104001.
[4] S. Ratynskaia, E. Thorén, P. Tolias, R.A. Pitts, K. Krieger, The MEMOS-U macroscopic melt dynamics code — benchmarking and applications, Phys. Scr. 96 (2021) 124009.
[5] M. Komm, S. Ratynskaia, P. Tolias, et al., On thermionic emission from plasma-facing components in tokamak-relevant conditions, Plasma Phys. Control. Fusion 59 (2017) 094002.
[6] M. Komm, P. Tolias, S. Ratynskaia, et al., Simulations of thermionic suppression during tungsten transient melting experiments, Phys. Scr. T 170 (2017) 014069.
[7] M. Komm, S. Ratynskaia, P. Tolias, A. Podolnik, Space-charge limited thermionic sheaths in magnetized fusion plasmas, Nucl. Fusion 60 (2020) 054002.
[8] P. Tolias, M. Komm, S. Ratynskaia, A. Podolnik, Origin and nature of the emissive sheath surrounding hot tungsten tokamak surfaces, Nucl. Mater. Energy 25 (2020) 100818.
[9] E. Thorén, S. Ratynskaia, P. Tolias, R.A. Pitts, The MEMOS-U code description of macroscopic melt dynamics in fusion devices, Plasma Phys. Control. Fusion 63 (2021) 035021.
[10] E. Thorén, S. Ratynskaia, P. Tolias, R.A. Pitts, K. Krieger, M. Komm, M. Balden, MEMOS 3D modelling of ELM-induced transient melt damage on an inclined tungsten surface in the ASDEX Upgrade outer divertor, Nucl. Mater. Energy 17 (2018) 194–199.
[11] K. Krieger, M. Balden, J.W. Coenen, F. Laggner, G.F. Matthews, D. Nille, V. Rohde, B. Sieglin, L. Giannone, B. Göths, A. Herrmann, P. de Marne, R.A. Pitts, S. Potzel, P. Vondracek, Experiments on transient melting of tungsten by ELMs in ASDEX Upgrade, Nucl. Fusion 58 (2018) 026024.
[12] E. Thorén, B. Bazylev, S. Ratynskaia, P. Tolias, K. Krieger, et al., Simulations with current constraints of ELM-induced tungsten melt motion in ASDEX Upgrade, Phys. Scr. T170 (2017) 014006.
[13] S. Mordijck, T.L. Rhodes, L. Zeng, A. Salmi, T. Tala, C.C. Petty, G.R. McKee, R. Reksoatmodjo, F. Eriksson, E. Fransson, H. Nordman, The WEST project: Current status of the ITER-like tungsten divertor, Fusion Eng. Des. 89 (7) (2014) 1048.
[14] https://amrex-codes.github.io/amrex/.
[15] W. Zhang, A. Almgren, V. Beckner, et al., Amrex: A framework for block-structured adaptive mesh refinement, J. Open Source Softw. 4 (37) (2019) 1370, http://dx.doi.org/10.21105/joss.01370.
[16] P. Tolias, Analytical expressions for thermophysical properties of solid and liquid tungsten relevant for fusion applications, Nucl. Mater. Energy 13 (2017) 42.
[17] P. Tolias, Analytical expressions for thermophysical properties of solid and liquid beryllium relevant for fusion applications, Nucl. Mater. Energy 31 (2022) 101195.
[18] Visit http://dx.doi.org/10.5281/zenodo.6778824 for the thermophysical property dataset.
[19] A. Herrmann, N. Jaksic, P. Leitenstern, H. Greuner, K. Krieger, P. de Marne, M. Oberkofler, V. Rohde, G. Schall, ASDEX Upgrade Team, A large divertor manipulator for ASDEX Upgrade, Fusion Eng. Des. 98–99 (2015) 1496–1499, http://dx.doi.org/10.1016/j.fusengdes.2015.02.007.

[20] M. Komm, R. Dejarnac, J.P. Gunn, A. Kirschner, A. Litnovsky, D. Matveev, Z. Pekarek, Particle-in-cell simulations of plasma interaction with shaped and unshaped gaps in TEXTOR, Plasma Phys. Control. Fusion 53 (2011) 115004.
[21] M. Komm, R. Dejarnac, J.P. Gunn, Z. Pekarek, Three-dimensional particle-in-cell simulations of gap crossings in castellated plasma-facing components in tokamaks, Plasma Phys. Control. Fusion 55 (2013) 025006.
[22] Y. Corre, A. Grosjean, J. Gunn, et al., Sustained W-melting experiments on actively cooled ITER-like plasma facing unit in WEST, Phys. Scr. 96 (2021) 124057.
[23] T. Eich, B. Sieglin, A. Scarabosio, A. Herrmann, A. Kallenbach, G. Matthews, S. Jachmich, S. Brezinsek, M. Rack, R. Goldston, Empirical scaling of inter-ELM power widths in ASDEX Upgrade and JET, J. Nucl. Mater. 438 (2013) S72–S77.
[24] J. Gunn, S. Carpentier-Chouchana, F. Escourbiac, et al., Surface heat loads on the ITER divertor vertical targets, Nucl. Fusion 57 (2017) 046025.
[25] M. Houry, et al., The very high spatial resolution infrared thermography on ITER-like tungsten monoblocks in WEST tokamak, Fusion Eng. Des. 146 (2018) 1104.
[26] J.W. Coenen, G. Arnoux, B. Bazylev, G.F. Matthews, A. Autricque, I. Balboa, M. Clever, R. Dejarnac, I. Coffey, Y. Corre, S. Devaux, L. Frassinetti, E. Gauthier, J. Horacek, S. Jachmich, M. Komm, M. Knaup, K. Krieger, S. Marsen, A. Meigs, P. Mertens, R.A. Pitts, T. Puetterich, M. Rack, M. Stamp, G. Sergienko, P. Tamain, V. Thompson, ELM-induced transient tungsten melting in the JET divertor, Nucl. Fusion 55 (2015) 023010.
[27] E. Thorén, P. Tolias, S. Ratynskaia, R.A. Pitts, K. Krieger, Self-consistent description of the replacement current driving melt layer motion in fusion devices, Nucl. Fusion 58 (2018) 106003.